Title

Emergent Ferroelectric Switching Behavior from Polar Vortex Lattice

Journal

Advanced Materials, 35(23)

ISSN

0935-9648

Authors

Behera, Piush

Parsonnet, Eric

Gómez-Ortiz, Fernando

et al.

Publication Date

2023-06-01

DOI

10.1002/adma.202208367

Metastable Switching Events in Polar Vortex Arrays

Piush Behera[1,2], Eric Parsonnet[3], Fernando Gómez-Ortiz[4], Vishantak Srikrishna[3], Peter Meisenheimer[1], Sandhya Susarla[1,2], Pravin Kavle[1,2], Lucas Caretta[1], Yongjun Wu[5], Zishen Tian[1], Abel Fernandez[1], Lane W. Martin[1,2], Sujit Das[6], Javier Junquera[4], Zijian Hong[5], Ramamoorthy Ramesh[1,2,3*]*

[1]Department of Materials Science and Engineering, University of California, Berkeley, Berkeley, CA 94720, USA.
[2]Materials Sciences Division, Lawrence Berkeley National Laboratory, Berkeley, CA 94720, USA.
[3]Department of Physics, University of California, Berkeley, Berkeley, CA 94720, USA.
[4]Departmento de Ciencias de la Tierra y Física de la Materia Condensada, Universidad de Cantabria, Cantabria Campus Internacional, 39005 Santander, Spain.
[5]Cyrus Tang Center for Sensor Materials and Applications, State Key Laboratory of Silicon Materials, School of Materials Science and Engineering, Zhejiang University, Hangzhou 310027, China
[6]Materials Research Centre, Indian Institute of Science, Bangalore 560012, India.

E-mail: rramesh@berkeley.edu, hongzijian100@zju.edu.cn

Keywords: Ferroelectrics thin films, topology, vortex state

Abstract: Topologically protected polar textures have provided a rich playground for the exploration of novel, emergent phenomena. Recent discoveries indicate that ferroelectric vortices and skyrmions not only host properties markedly different from traditional ferroelectrics, but also that these properties can be harnessed for unique memory devices. Using a combination of capacitor-based capacitance measurements and computational models, we demonstrate that polar vortices in dielectric-ferroelectric-dielectric trilayers exhibit classical ferroelectric bi-stability together with the existence of low-field metastable polarization states. This behavior is directly tied to the in-plane vortex ordering, and we show that it can be used as a new method of non-destructive readout-out of the poled state.

1. Introduction

The recent discovery of ferroelectric (FE) polar textures in $(PbTiO_3)_n/(SrTiO_3)_n$ (PTO/STO) superlattices has opened the door to realization of emergent phenomena not accessible in traditional ferroelectric materials. Through careful control of the elastic, electrostatic, and gradient boundary conditions, polar textures such as vortices[1], skyrmions[2], and merons[3,4] can all be formed within the PTO/STO superlattices. The vortices, in particular, have been shown to host numerous novel properties including negative capacitance[5,6], chirality[7–9], and most recently phonon-like collective dynamics.[10] One of the most important remaining pursuits is how to harness the exotic behavior of the polar vortices for device applications.

Multiple studies have been performed, focusing on the transformation of the polar vortices under an applied electric field using *in situ* transmission electron microscopy (TEM),[11,12] piezoresponse force microscopy (PFM),[13] nonlinear optics,[9,13] and in computational models and simulations.[8,9,13] The majority of these studies have focused on the out-of-plane switching behavior (in response to out-of-plane electric fields) using local imaging techniques to measure the transformation from a vortex state to a polarization wave state and finally to a single *c*-domain state.[12] When measuring the net change in polarization as an electric field is applied (*i.e.,* as in a polarization-electric field hysteresis loop), however, the system displays minimal hysteresis with little saturation (Figure S1). More recent studies focused on the in-plane switching behavior, on the other hand, reveal that the vortex system displays bi-stability, reminiscent of classical ferroelectrics.[9,11] The appearance of bi-stable behavior allows for the storage of memory, for example, as either a 1 or 0 based on the state on whether the system is in a positively poled, $+P$, or negatively poled, $-P$, state, particularly at low electric fields, as we show in this work.

Traditional ferroelectric random access memories (FeRAM) have long been touted for their promise as a non-volatile (NVRAM) form of memory storage with high operation speeds, low energy costs, and high endurance compared to other forms of NVRAM.[14–16] In capacitive based FeRAM, one can address memory by poling the system to a state $+¿P$ or $-P$ state. Unfortunately, one can only measure changes in polarization, so to read out the state of the material one must switch the polarization state of the material by applying a field larger than the coercive field. The change in state from $-P$ to $+¿P$, however, means that the bit has now been altered and must be readdressed to the $-P$ state if one wants to re-read the data.[14–16] This so-called destructive readout can be overcome by using a more complicated device geometry such as in ferroelectric field-effect transistors (FeFET), where a ferroelectric material is included in the gate stack, or by measurement of tunneling currents through ultrathin ferroelectrics in a ferroelectric tunnel junction (FTJ). But, to date, non-destructive readout has not been achieved in the simplest FeRAM architectures and these other devices often come with their own challenges due poor endurance properties, depolarization effects, and interface quality.[16] Here, we delve deeper into the origins of the bi-stable, in-plane polarization of the vortex structure and show how its unique switching behavior can be harnessed for non-destructive, capacitor-based memory.

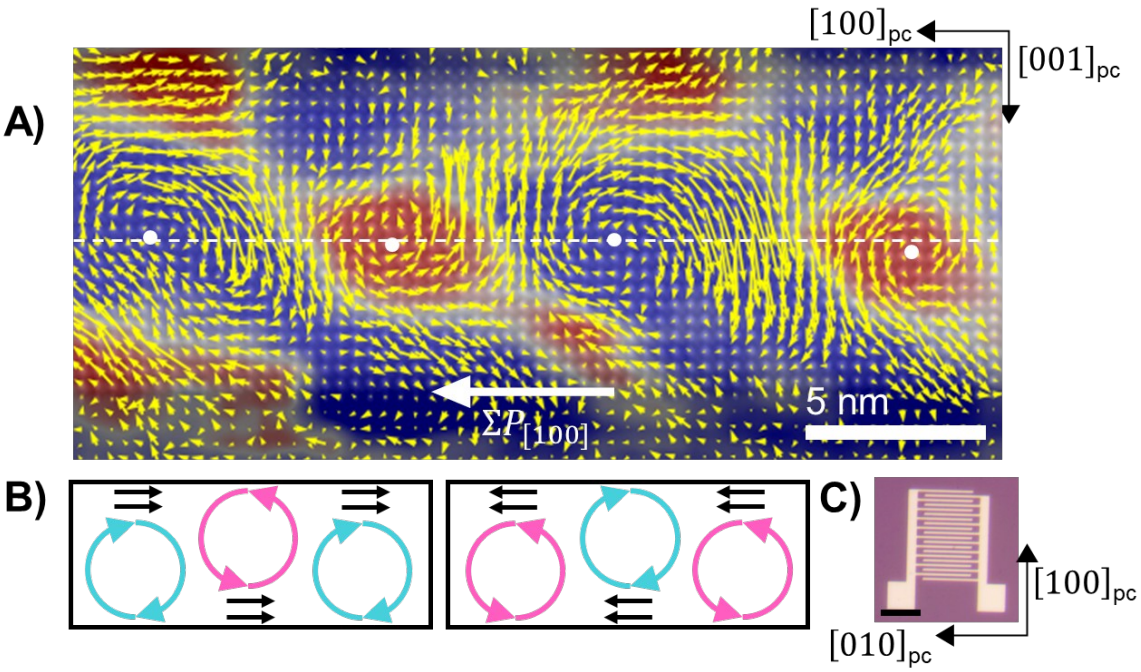

Figure 1 (A) High resolution scanning transmission electron microscopy (HRSTEM) showing polarization textures in $PbTiO_3/SrTiO_3$ tri-layers. The yellow arrow represents the local displacement of the A or Pb sites. The curl of the displacement is shown as the red/blue contrast. The zig-zag configuration/buckling can be observed by the off-centering of the vortex cores, marked by white circles, with the center line of the PTO layer, marked by the white dashed line. Direction of the net polarization is represented by the white arrow. (B) Schematics of the two possible polarization states of the vortices, with blue, clockwise vortices and pink, counter-clockwise vortices (C) In-plane interdigitated electrode used for capacitive measurements. Scale bar is 60 μm.

The origins of the in-plane bi-stability are directly tied to the ordering of the vortex lattice. Within the plane of the film and withing each PTO layer, neighboring vortices rotate in opposite directions, forming a lattice of alternating clockwise and counterclockwise vortices. Under the tensile strain imposed by the substrate ($DyScO_3$), the development of a mixture of out-of-plane and in-plane polarization components are favored. To accommodate the in-plane polarization the vortices off-center, where the vortex cores of neighboring vortices displace (slightly) in the out-of-plane direction within the PTO layer towards the interface with STO in an alternating up-down fashion (Figure 1A). The alternating rotation in conjunction with the off-centering leads to the formation of a spontaneous, net in-plane polarization along the $[100]_{pc}$ (Figure 1B). Moreover, this net in-plane polarization can be tuned by application of external in-plane electric fields along the $[100]_{pc}$ (*i.e.*, perpendicular to the long-axis of the vortex tube). When such fields are applied, the net in-plane polarization, which is coupled to the vortex offset ordering, can be switched.[9] In comparison to classical models of ferroelectricity where a spontaneous, switchable polarization emerges due to the softening of an optical phonon mode; this net in-plane polarization is driven by a strain-induced softening of the recently discovered "vortexon" modes.[10,17] While previous work has already demonstrated this behavior,[9] the current work realizes the existence of low-field, metastable switching events. These previously unnoticed switching events can be used to overcome one of the fundamental challenges with ferroelectric memory: the requirement of a destructive readout mechanism.

For this study, symmetric $(SrTiO_3)_{20}/(PbTiO_3)_{20}/(SrTiO_3)_{20}$ trilayers were grown on $DyScO_3$ (110) [*i.e.*, $(001)_{pc}$] substrates using reflection high-energy electron diffraction (RHEED)-assisted pulsed-laser deposition (Methods). The polar-vortex structure was confirmed using high-angle annular dark field scanning transmission electron microscopy (HAADF-STEM), where atomic-scale ionic displacements can be measured, as compared to the cubic structure, revealing the vortex structure (**Figure 1A**). For further investigation into the switching behavior of the polar vortices a combination of experimental techniques and computational modelling are used to focus on origins of the switching mechanism and finally we reveal how this behavior can be functionalized for a novel form of FeRAM.

2. Results and Discussion

2.1. In-Plane Polarization Response

Using interdigitated electrode structures (Figure 1C), we apply in-plane electric fields along the $[100]_{pc}$. As has been previously demonstrated,[9] we observe a hysteretic behavior between the in-plane polarization and the applied field (**Figure 2A**). This change in polarization with electric field (PE loop) is due to a reversal in the off-centering pattern or the buckling pattern of the vortices seen in Figure 1A.[9] Additionally, the PE loop clearly displays pinching (marked by the grey arrows in Figure 2A) at fields lower than the coercive field.

Pinched PE loops are not uncommon in ferroelectrics,[18–22] and such features are often attributed to the creation of a deep pinning potential for domain walls,[18,20] but it may also arise due to an electric-field driven phase transformation[19,21] or due to defect dipoles.[20,22] Here, we distinguish two switching events, henceforth called "major" and "minor". The major-switching event occurs for fields larger than the coercive field (~25 kV/cm), where the out-of-plane offset of the

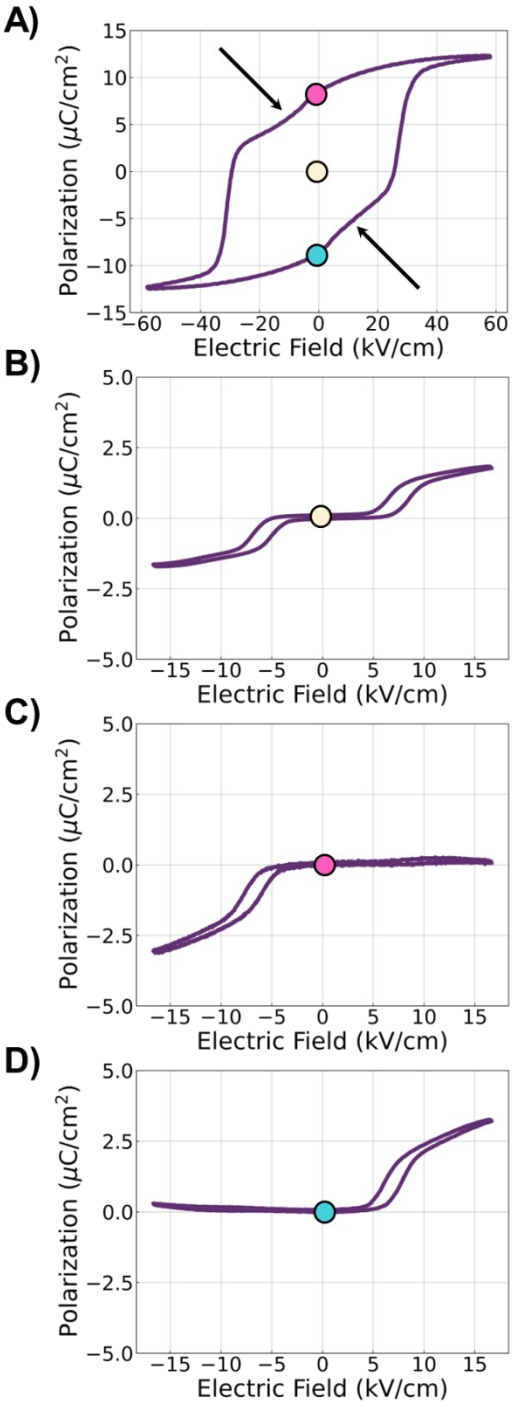

Figure 2 (A) Major PE loop (B-D) Minor PE loops taken for as-grown sample (B), positively poled sample (C), and negatively poled sample (D). We note that the dielectric component of each loop has been subtracted, see Figure S2 for raw data. Additionally, we can only measure the change in net polarization of the material, hence why at zero-field the 'polarization' is at zero despite the minor loops, (C) and (D), being taken at poled states.

vortices is reversed and consequently the net in-plane component of the polarization also changes direction. At lower fields (< 25 kV/cm), minor-switching events also take place wherein the system displays PE loops reminiscent of antiferroelectric behavior; with hysteresis at a non-zero field and a remnant polarization of zero (Figure 2B). We note that traditionally, minor-PE loops are referred to PE loops taken at sub-switching fields where the one achieves partial switching of the ferroelectric; it typically does not refer to a different switching event, as it does here. When performing PE measurements below the coercive field for as-grown trilayers, we observe hysteresis when applying both a positive and a negative field (a so-called double loop; Figure 2B); however, strikingly, upon poling the sample the minor PE loops become anisotropic. Poling to the positive (+*P*) state leads to a minor loop with only hysteresis at negative fields (Figure 2C), and poling to the negative (-*P*) state leads to hysteresis upon the positive side (Figure 2D).

Since, these minor loops become anisotropic upon poling, we can harness this anisotropy for readout of the poled state. If the system is in the +*P* (-*P*) state we know that the minor loop will display hysteresis only at negative (positive) fields, thus allowing for the state to be read without having to apply a field larger than the coercive field which would destroy the state. Additionally, because the minor loops relax (*i.e.,* display no remnant change in polarization), the state of the system remains unaltered after measuring the minor loop. Thus, these minor loops can be harnessed for a low-field, non-destructive readout mechanism of the poled state.

2.2. Harmonic Analysis

The behavior of classical dielectrics under an applied electric field are typically well described by their intrinsic-lattice response, leading to rather weak nonlinear effects such that they can be described as "linear" dielectrics. The presence of defects, dipole clusters, or domains, as is the case of ferroelectrics, however, can lead to strong nonlinear polarization response.[23] By studying a material's nonlinear behavior one can better understand the dynamics of the materials and the physical origins of the material's nonlinearities. To investigate the origins of both the major- and minor-switching events, we turn to harmonic analysis, a technique by which we measure the polarization response for different harmonics of the drive-signal frequency.

Typically, to understand the switching behavior of a ferroelectric a periodic electric field, $E(t)$, is applied and the total change in polarization, $P(t)$, is measured. This is then plotted as $P(E)$ loops; however, quantitative information about the details of the switching process using such loops can be difficult to extract. Given that the driving field is periodic (in our case sinusoidal), the polarization response will also be periodic in nature and can thus be expressed as a sum of individual Fourier components:[23]

$$P(t)=\sum_{n=1}^{\infty} P^{|n|}\sin\left(n\omega t+\delta_n\right) \tag{1}$$

where $P^{|n|}$ is the amplitude of the change in net polarization for the n^{th} harmonic, t is time, n is an integer corresponding to each harmonic, ω is the drive frequency, and δ is the phase shift.[23] Measurement of each of these Fourier components allows for the recreation of the total PE loop that is measured, but in general it has been found that measurement of the first three components provides sufficient data.[23]

In practice we use a lock-in amplifier (Methods) to measure the polarization response at different, specific harmonics of the drive frequency while applying an AC field of increasing amplitude.[23] By tracking how the amplitude and phase changes with excitation, we

can measure subtle changes in the nonlinear behavior and, therefore, the switching mechanism. In particular, the phase shift, δ_n, provides insight into the switching mechanism. As described in Ref. [23], the out-of-phase component of the fundamental, $n = 1$, polarization response determines the total area inside the PE loops. All higher harmonics either change the shape of the loop or redistribute its area. For higher-order, odd harmonics, a phase shift of 0° or -180° indicates an in-phase response (with respect to the driving field) and is characteristic of a reversible response that only bends the shape of the overall PE loop; whereas, a phase shift of -90° indicates an irreversible, out-of-phase response that redistributes the hysteresis area within the PE loop.[23] For even-numbered components the opposite holds true, where the out-of-phase component indicates reversible behavior and the in-phase component indicates the irreversible behavior of that harmonic response.[23] For detailed information on these approaches, the reader is directed to a review article on the measurement and interpretation of nonlinear polarization response by *Riemer et. al.*[23]

Using such a lock-in based technique, we measured the polarization response of the first three harmonic when applying AC-fields of increasing amplitude along the $[100]_{pc}$ (**Figure 3A**). Though there is little change in the phase shift in the first two harmonics, the third harmonic, $n = 3$, shows significant changes as the field amplitude is increased. Previous work has shown that the phase of the third harmonic, $n = 3$, strongly depends on the active switching mechanism and can provide insight into the switching dynamics.[23,24] There are three key events seen in the third harmonic data (Figure 3A). First, upon applying a 6 kV/cm field we see an immediate drop of the phase of the third harmonic to -180° (for values smaller than 6 kV/cm the signal is too small for accurate measurements). Second, the phase shift of the third harmonic drastically increases around 12 kV/cm up to -20°. Third, there is a steady decrease at fields higher than 15 kV/cm, tending to a plateau value of -80°. By comparing this data to the PE-loop data (Figure 2), we can associate the change of the third harmonic between 5 and 12 kV/cm to the minor-switching event and the subsequent drop of the third harmonic beyond 15 kV/cm to the major-switching event (Figure 2A), demonstrating that both of these switching events have distinct driving mechanisms.

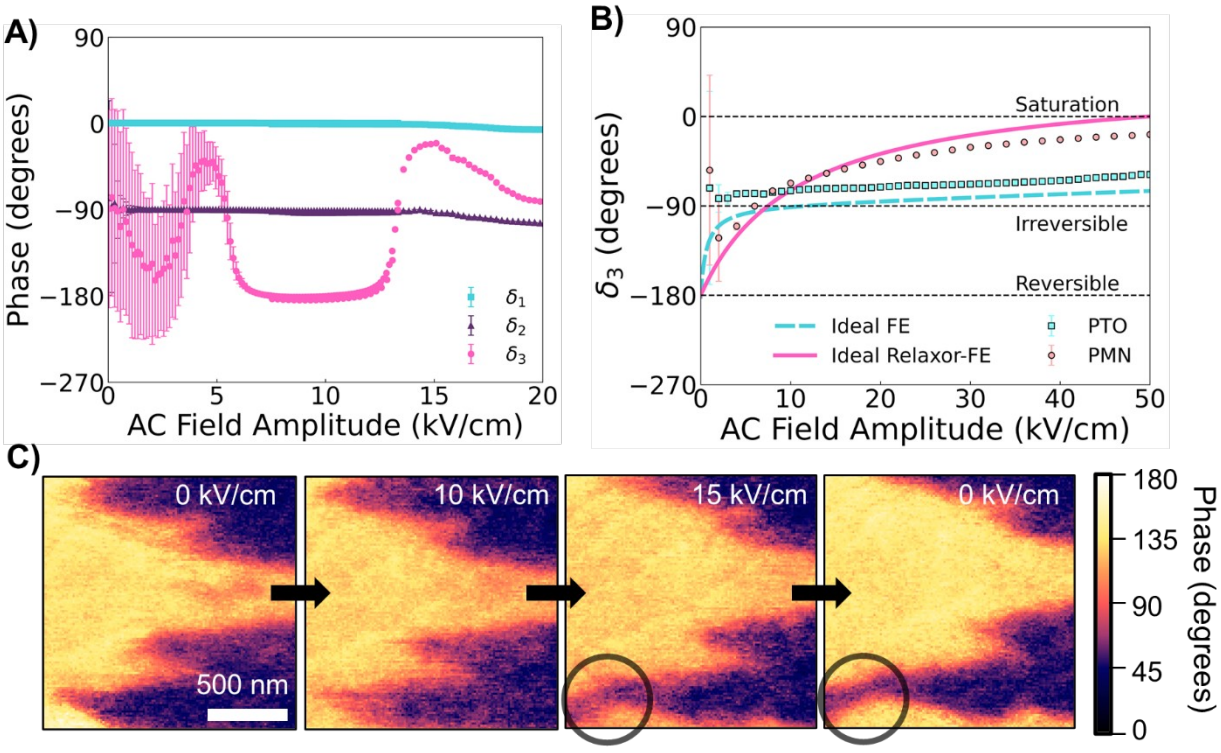

Figure 3 (A) First (blue), second (purple), and third (pink) harmonic measured along the in-plane polarization of the vortices at 10kHz. Error bars represent standard deviation of 10 subsequent measurements (B) Third harmonic measured for a 50 nm PTO (blue squares) and 100nm PMN (pink circles) sample. Lines are guide to eyes for expected behavior for classical ferroelectrics (blue dashes) and relaxor ferroelectrics (solid pink) based on previous literature. [24] (C) *In situ* PFM measurement of vortex sample. Contrast arises from domains of different in-plane polarization due to difference in buckling pattern. As the field is increased, we see no change in the domain structure until ~15 kV/cm at which point the domain wall irreversibly moves (circled in grey).

For comparison, we show the behavior of the third harmonic for reference samples of ferroelectric PTO and the relaxor $PbMn_{1/3}Nb_{2/3}O_3$ (PMN) (Figure 3B). In the case of PTO, we observe the third harmonic slowly rising from -90°. This behavior is expected of classical ferroelectrics and can be understood using the Rayleigh model,[25,26] which is conventionally used to describe how domain-wall movement under an applied field affects the evolution of the phase of the third-harmonic response. In a random-pinning potential, at low-fields domain walls will, macroscopically remain stationary but will vibrate within the pinning potential. The vibration of the domain wall within the pinning site is fully reversible and a phase of -180° is seen (at low fields our signal is too small to capture this regime). As the field-amplitude increases, domain walls can move from one pinning site to another in an irreversible fashion. This irreversible movement of domain walls leads δ_3 to change from -180° to -90°. This behavior has been seen in numerous ferroelectric systems including $BaTiO_3$;[24] however, this is not the only commonly observed behavior. When similar measurements are performed on soft ferroelectrics or relaxors, the phase shifts from -180° directly to 0°; resembling our measurement for PMN.[23,24,27] Such a behavior cannot be ascribed to the Rayleigh model since it indicates a fully reversible switching mechanism, unrelated to domain-wall motion. Previous studies have generally ascribed this to the movement of polar nanoregions (PNRs) in a paraelectric matrix and this has been observed in multiple systems including $Ba_{0.2}Sr_{0.8}TiO_3$ (BSTO), $PbSc_{0.5}Ta_{0.5}O_3$, as well as PMN.[24,27–29]

Using these models for comparison, we can ascribe the behavior at high fields in our vortex system, where δ_3 decreases towards -90° above 12 kV/cm, as evidence of irreversible domain-wall motion as described by the Rayleigh model. Further evidence is shown through *in situ* lateral PFM measurements (Figure 3C). Starting from the initial state, one sees contrast arising from domains of opposite buckling patterns and thus opposite in-plane polarization.[9] As the field increases, we see no change in domain structure until we reach 15 kV/cm. A domain wall from the -*P* (blue) poled domain suddenly expands, and this motion remains even after removal of the field. Importantly, we see no change in the domain structure at fields lower than 15 kV/cm, which indicates that the minor-switching behavior, where δ_3 goes from -180° to nearly 0°, cannot be ascribed to the motion of domain walls. Further, *ex situ* PFM measurements also corroborate this absence of domain-wall motion after the minor-switching mechanism is activated (Figure S7 and S8).

Based on the PFM studies and the behavior of δ_3 at low-fields, we can rule out domain-wall motion as a possible origin of this observation; rather it displays a relaxor-like response despite the absence of traditional polar nanoregions. This suggests that δ_3 at these low fields may be related to the motion of the vortices themselves. Furthermore, we note that at even lower fields (< 7 kV/cm), we see saturation of another mechanism not visible in the PE loop. Though noisy due to the low signal magnitude (Figure 3A), the δ_3 is about -40° around 5 kV/cm, before a sudden drop to -180°. This may indicate that an even lower field

switching mechanism is approaching saturation; however, due to the low signal we cannot comment on the true nature of this behavior.

2.3. Mechanism Behind the Minor Switching Event

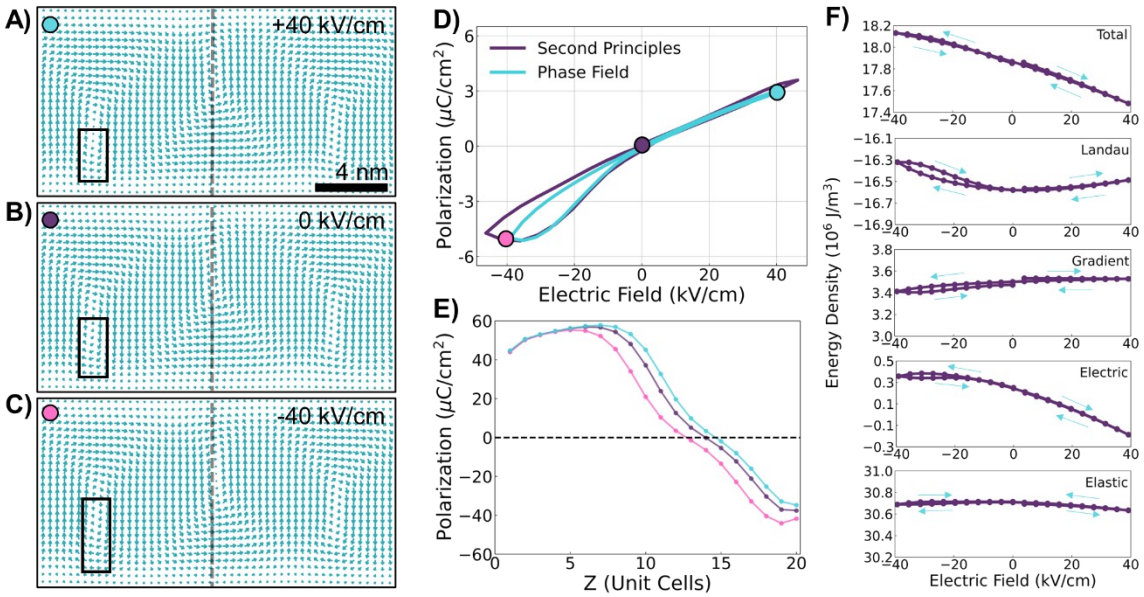

Figure 4 (A-C) Phase field model of vortices at +40 kV/cm (A), 0 kV/cm (B), and -40 kV/cm (C). Black boxes are drawn from vortex centroid to PTO/STO interface and are used to demonstrate how the vortices shift slightly as the field is applied. (D) Minor PE loop for as positively poled vortex system calculated using second principles (purple) and phase field modelling (blue). (E) Line scan of vortex (dashed lines in A-C) showing the in-plane polarization vortex position at 0 kV/cm (purple), -40 kV/cm (pink), and +40 kV/cm (blue). (F) The evolution of the total energy density and its components as a function of field as calculated through phase-field modeling.

To understand the microscopic origins of the minor switching behavior, a combination of second-principles calculations and phase-field simulations was used to examine how the atomic structure of the vortices change at these low-fields (**Figure 4A-C**). In both approaches, we can recreate the same polar-vortex lattice and simulate how the vortex structures change under an applied field and calculate their net in-plane polarization (Figure 4A-C). Additionally, one can see that both second-principles calculations and phase-field simulations are able to recreate the anisotropic minor loop for a positively poled sample (Figure 4D; see Figure S8 and S9 for phase field simulations of the negatively poled minor loop and the major loop).

Starting from a positively poled system under zero external field (Figure 4B), the clockwise (CW) rotating vortices lie above the midpoint of the PTO layer and the counterclockwise (CCW) vortices lie below the midpoint, leading a positive net-in plane polarization. We note that for the PE loop we subtract this net polarization such that $P_x = 0$ for zero external field as seen by the purple circle in Figure 4D. Now as an external electric field is applied opposite to the in-plane polarization (*i.e.,* along the negative x direction; Figure 4C), the vortices shift towards the midpoint of the PTO layer, thereby reducing the net polarization. As the vortices shift towards the midpoint of the PTO layer, a row of local dipoles above/below the CW/CCW vortices must reverse their direction, noted by the black boxes in Figure 4A-C, and for every row of unit cells whose polarization is reversed the CW/ CCW vortices shift up/down by one unit cell (Figure 4C).[30] It is this shifting of the vortices

by a few unit cells produces the hysteresis in the minor loops theoretically predicted (Figure 4D) and seen experimentally (Figure 2C). As the field is reduced again, the vortices remain in their displaced state until the field is no longer large enough large enough to support the displaced vortex configuration, as further illustrated in Figure S10.

Though these same effects can occur when a field is applied along the net in-plane polarization (Figure 4A), one sees minimal hysteresis at positive fields for this configuration (Figure 4D). This is due to the fact that a field parallel to the in-plane polarization will shift the vortices towards the PTO/STO interface, where there is much less room for the vortices to displace before destruction of the vortex state. Therefore, the shifting of the vortices toward the PTO/STO interface is much less favorable and it is a classical polarization extension that dominates the polarization response. Thus, the anisotropy seen in the minor loops is a direct consequence of the buckling pattern of the vortices

These vortex displacements are further illustrated in Figure 4E, where the x-component of the local dipoles along the vertical dashed line crossing the upper counter-clockwise vortex core shown in Figure 4A-4C is displayed. At the center of the core, this in-plane component of the polarization vanishes. Due to the remanent offset in the absence of external field, the core is not located at the center of the PTO layer, but at a higher position, as shown (purple curve, Figure 4E). A positive electric field essentially does not modify this position (small differences between the blue and purple curves, Figure 4E). However, a negative field large enough to produce the switching of a row of local dipoles produces the displacement of the vortex core towards the center of the PTO layer, as demonstrated by the relatively large shift between the pink and purple curves (Figure 4E).

Furthermore, by examining the energy density of the vortex system as a function of the external electric field (Figure 4F), the total energy density of the system displays little hysteresis even within the hysteretic regimes of the PE loop. Despite the vortex system being in different state as the field amplitude is increased and decreased, the total energy remains nearly identical due to the individual components of the energy density delicately balancing each other out. As a row of polarization is switching there is an increase in the Landau energy, but this is compensated by decreases in both the gradient and electric energy terms (Figure 4F). Thus, these two slightly different vortex states remain close in energy until the field is finally turned off such that the system relaxes back to its initial state, indicating that vortex system exists in a double well structure alongside numerous vortex cores states that are close in energy to the ground state.

2.4. Mechanism Behind the Minor Switching Event

Having shown the origin of the minor-switching behavior, here we demonstrate how such behavior can be harnessed for a novel, non-destructive readout of the ferroelectric state. As previously described, a capacitive FeRAM requires a destructive readout mechanism to determine if the system is in the $+¿P$ or $-P$ state.[14–16] With the vortex system, one can use the metastable, anisotropic minor loops as a way of determining the poled state of the system at fields well below the switching field. Whether the minor loops are hysteretic at positive or negative fields can be used as a nondestructive readout of the state of the major loop, for example by applying a small positive bias to the system, less than the coercive field of the major loop and larger than the coercive field of the minor loop, one would measure a switching current for a negatively poled sample and no switching current for a positively poled sample (for the current versus field response see Figure S11). Furthermore, since the minor loops show no remnant change in polarization one can continue to read-out the system without altering the overall poled state. Indeed, these minor loops can be read continually for up to 10^{10} cycles without any noticeable changes (Figure S12).

Now we utilize the readout mechanism enabled by the anisotropic minor loops to measure the switching speed of the major switching event. The pulse sequence used for measurement of the switching speed is illustrated in **Figure 5A**. We use the triangular waveforms to measure the minor PE loops (Figure 5B) before and after applying a switching pulse of variable pulse width and pulse amplitude (Methods). By taking the difference between the saturation polarization of the minor loop at positive fields ($\Delta P_s^{+¿¿}$, noted by the black arrow in Figure 5B), we can measure to what degree the system was switched by the applied pulse. The degree of switching, $\Delta P_s^{+¿¿}$, is measured for a wide range of pulse widths and amplitudes (Figure 5C). Clear switching behavior (indicated by blue) is seen from 500 ms to as low as 100 ns (see Figure S13 for switching data out to 100 s). We note that even for 500 ms pulse widths, the switching field is well above 11.67 kV/cm, the field amplitude used for measurement of the minor PE loops (raw data of minor loops is provided, Figure S13).

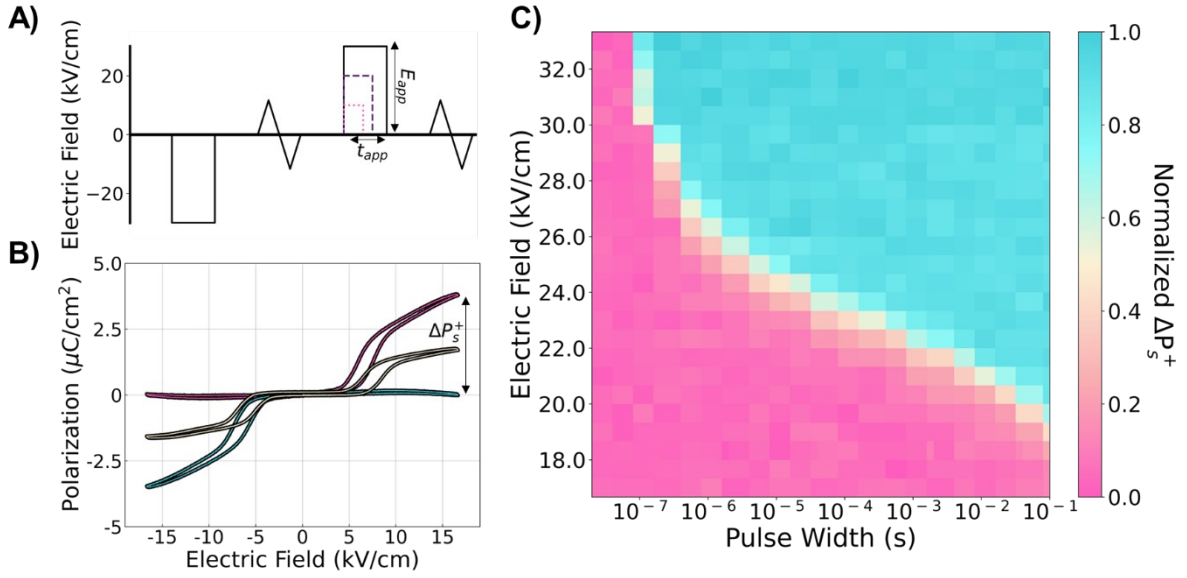

Figure 5 (A) Pulse sequence used for switching measurement. First a -30 kV/cm, 1ms pulse is used to set the material in the negative state. A minor PE loop is then taken with a bipolar triangle wave of amplitude of 11.67 kV/cm to confirm the state. A positive switching pulse of variable time and amplitude is applied. Finally, another minor PE loop is taken to measure if the system has switched or not. (B). Representative curves for whether the materials did not switch (pink), partially switched (yellow), or fully switching (blue). Measuring the difference in polarization at positive field between the first and second PE loop allows us to calculate the relative degree of switching. See Figure S14 for example of raw data. (C) The normalized degree of switching, as quantified by $\Delta P_s^{+¿¿}$, as a function of pulse width and pulse amplitude/electric field. Dark pink indicated no-switching, whereas dark blue indicated full switching.

Additionally, we see that as the pulse width is increased, the required switching field decreases. This decay of switching time with electric field is further indication that the major switching event is driven by the nucleation and growth of domain walls as seen in both the harmonic analysis and PFM measurements (Figure 3). Furthermore, we find that by fitting the switching time as a function of field to Merz's law (Figure S14, Supplementary Section A), an empirically derived model based on nucleation and growth of domains,[31,32] it would take over 700 years to change the poled state of the system given that one reads the minor loops with a field amplitude of 12.5 kV/cm. Therefore, usage of the minor-switching event would

even improve upon data retention due to a lower requirement of the field needed to read the state of the system.

3. Conclusion

Here we have demonstrated how the ordering of the ferroelectric vortices gives rise to novel functionality and switching behavior. Due to the buckled nature of the vortices, the emergence of fully switchable in-plane polarization gives the bistability required for nonvolatile memory applications. Furthermore, at lower fields we find previously unrealized switching events due to unit-cell level, metastable displacements of the vortices. This metastable behavior comes as a direct consequence of confinements of the vortices, as both the vortex size, vortex displacements, and ferroelectric layer thickness are all similar length scales. One can harness these metastable switching events for the non-destructive readout of the in-plane poled state in a simple capacitor structure. While there is clearly more work needed to functionalize this behavior, this confinement-based approach may be applicable to other ferroelectric systems where one can use the discrete motion of confined domain walls for non-destructive readout. Additionally, the importance of the vortex ordering in its novel properties and functionalities should lead to interest in the ordering of other polar topological defects such as merons and skyrmions.

4. Experimental Section/Methods

Sample Growth STO/PTO/STO

The $(SrTiO_3)_{20}/(PbTiO_3)_{20}/(SrTiO_3)_{20}$ trilayers were synthesized on single-crystalline DSO $(110)_o$, where $(110)_o=(001)_{pc}$, substrates via RHEED-assisted pulsed laser deposition (KrF laser) as described in Ref. [1].

Sample Growth PTO

50nm $PbTiO_3$ samples were grown using pulsed-laser deposition in an on-axis geometry with a target-to-substrate distance of 60 mm, using a KrF excimer laser (248 nm, LPX 300, Coherent) as described in Ref. [33].

Sample Growth PMN

50 nm $Ba_{0.5}Sr_{0.5}RuO_3$ /100 nm $PbMg_{1/3}Nb_{2/3}O_3$ /50 nm $Ba_{0.5}Sr_{0.5}RuO_3$ heterostructure was deposited on LSAT (001) substrate (CrysTec GmbH) via pulsed-laser deposition using a 248-nm-wavelength KrF excimer laser (LPX-300, Coherent). The $Ba_{0.5}Sr_{0.5}RuO_3$ bottom electrode was deposited from a ceramic target (Praxair) under heater temperature 750 °C, oxygen pressure 20 mTorr, laser fluence 2.0 J cm^{-2}, and laser repetition rate 4 Hz. The $PbMg_{1/3}Nb_{2/3}O_3$ film was deposited from a ceramic target with 10% lead excess (Praxair) under heater temperature 600 °C, oxygen pressure 200 mTorr, laser fluence 1.8 J cm^{-2}, and laser repetition rate 2 Hz. The top electrode was grown under the same conditions as the bottom electrode but heater temperature was kept at 600 °C. Following the growth, the chamber was cooled down in oxygen atmosphere of 760 Torr.

Device Fabrication

The electrodes were patterned using UV lithography using a Heidelberg MLA150 Maskless Aligner in the Berkeley Marvell NanoLab at CITRIS, with AZ MiR 701 Photoresist, followed by Pt sputtering (80 nm). The Pt was then lifted off via a ~12 hour soak in 1-methyl-2-

pyrrolidone (NMP). For these devices the finger length was 120 μm, the number of fingers was 20, and finger spacings of 10, 5, 3, and 1 μm were used.

PE Loop and IV Curve Measurements

PE loops and IV curves were taken using a Precision Multiferroic Tester (Radiant Technologies), measured at 1 kHz unless stated otherwise. IV curves for the minor loop were taken after averaging 100 loops due to low signal.

Harmonic Analysis Measurement

The amplitude and phase shift of each harmonic was measured using a Stanford Research System SR830 Lock-In Amplifier, while applying a 10 kHz sine wave of increasing amplitude. Measurements of STO/PTO/STO trilayers were done on in-plane capacitors at room temperature. Measurement of PTO and PMN were done in an out-of-plane geometry and measurements for PMN were done at 178K, below the material's $T_{max,}$ so that the transition could be more easily measured. Data acquisition and analysis was done using *ekpy*.[34]

Switching Speed Measurement

For this measurement we used four wave forms to measure the switching speed of the materials. First, a -30 kV/cm, 1ms pulse was used to set the system in the −P state. Second, a 1kHz bipolar triangle wave with a 11.67 kV/cm peak amplitude was used to measure the minor PE loop. Third, a positive pulse of variable width and amplitude was used to 'switch' the material. Finally, another minor loop was taken with the same conditions as the first PE loop. Additionally, a one-second delay was used between each waveform. The degree of switching ($\Delta P_s^{+¿¿}$) was measured by taking the difference of the saturation polarization at positive fields between the first and second PE loop, $\Delta P_s^{+¿=P_s^{+,1}-P_s^{+,2}¿}$. Pulses were generated using a pulse Berkeley Nucleonics (no. BN 765) pulse generator, while PE loops were measured using a Precision Multiferroic Tester (Radiant Technologies). Data acquisition and analysis was done using *ekpy*.[34]

In Situ and Ex Situ PFM

Using an atomic force microscope (MFP-3D, Asylum Research), we conducted dual a.c. resonance tracking lateral PFM using a conductive Pt/Ir-coated probe tip (NanoSensor PPP-EFM) to image the in-plane domain structures.[9] For in situ measurements, in-plane capacitors were wire bonded to a chip carrier and a dc bias was applied using a Keithley 2400 Sourcemeter. For ex situ measurements, voltage pulses were applied between measurements using a Precision Multiferroic Tester (Radiant Technologies).

Endurance Cycling

Endurance cycling measurements were performed up to 10^{10} cycles using a 500 kHz triangle wave with a peak amplitude of 20 kV/cm with a Precision Multiferroic Tester (Radiant Technologies).

TEM Measurement

All the trilayer samples were polished using a were mechanically polished using a 0.5° wedge. The samples were subsequently Ar ion milled in a Gatan Precision Ion Milling System, starting from 3.5 keV at 4° down to 1 keV at 1° for the final polish. The subsequent high resolution scanning transmission electron microscopy (HR-STEM) was performed using

the double aberration corrected FEI microscopes at 300 kV, 30 mrad convergence angle and 50 pA beam current.

The data processing was performed using the "finding polarization vector" in TopoTEM.[35] In summary, all the A sites were found using atom detection. Afterwards, all the detected atoms were divided in the zone vector planes. The deviation in local A-displacement were found by taking the difference between the local A site displacement and the corresponding average displacement in the local zone axis plane. The displacement vectors were further interpolated into a grid Cartesian grid and then differentiated to obtain strain tensor maps. The infinestimal rotation or the curl of the displacement of vortices was calculated using the following equation:

$$\theta = \frac{1}{2}\left(\frac{\partial u}{\partial y} - \frac{\partial v}{\partial x}\right)$$

Phase-Field Simulations

Phase-field simulations are performed to investigate the switching kinetics of the $(STO)_{16}/(PTO)_{16}/(STO)_{16}$ trilayer on a DSO substrate. The spontaneous polarization vector ($\vec{P}$) is employed as the primary order parameter, governed by the time-dependent Ginzburg-Landau (TDGL) equations:[36–38]

$$\frac{\partial \vec{P}}{\partial t} = -L\frac{\delta F(\vec{P}, \nabla \vec{P})}{\delta \vec{P}}$$

where t and L are the evolution timestep and kinetic coefficient, respectively. The total energy F has the contributions from the Landau, elastic, electric, and gradient energy densities, i.e.,

$$F = \int \left(f_{Land} + f_{elas} + f_{elec} + f_{grad}\right) dV$$

Detailed expressions for the energy densities and the materials parameters can be found in previous literatures.[36–40]

The simulation system is discretized into a three-dimensional mesh of $400 \times 400 \times 100$, with each grid representing 0.4 nm. Periodic boundary condition is applied along the inplane dimensions, while a superposition method is used in the out-of-plane direction.[40] Along z direction, the thickness of substrate, thin film, and air is set as 30, 50, and 20, respectively. Thin film elastic boundary condition is employed where the out-of-plane stress is fixed to zero on the thin film top, while the out-of-plane displacement on the substrate bottom sufficiently far away from the electrode/superlattice film interface is set as zero. An iterative perturbation method is used to solve the elastic equilibrium equation.[42]

Second Principles Simulations

The second-principles simulations were performed using the same methodology presented in previous works,[43,44] as implemented in the Scale-Up package.[44] The interatomic potentials, and the approach to simulate the interface, are the same as in [8]. We impose an epitaxial constraint assuming in-plane lattice constants of a = b = 3.911 Å forming an angle of α= 90°. This corresponds to a small tensile epitaxial strain of +0.25% with respect to the reference structure used in previous works (where a = b = 3.901 Å) and mimics the mechanical boundary conditions imposed by the DSO substrate and the ones used in [9]. This epitaxial condition favors the onset of an in-plane component of the polarization, which couples with the offset of the cores of the vortices.

For computational feasibility, we have focused on a simulation supercell made from a periodic repetition of 2n × 1 × 2n elemental perovskite unit cells, sufficiently large to allocate a pair of counterrotating vortices. At low temperatures, the vortex phase is invariant along the

axial direction therefore this simplification does not alter the model while speeds up the calculations. For a given value of the electric field along x, we solved the models by running Monte Carlo at T=0K, typically comprising 10,000 thermalization sweeps, followed by 10,000 sampling sweeps where we averaged the polarization along x. To perform the hysteresis loop, we started from a positively poled relaxed structure at zero electric field. Afterwards, we used the relaxed structure as seed for the next calculation changing the value of the electric field ranging from –46 to 46 kV cm^{-1} in steps of 5.14 kV cm^{-1}.

Statistical Analysis

PE loop measurements include subtraction of the linear dielectric component as presented in Fig. S2. Subtraction was done by first performing a linear fit to the center of the minor loops or the point of saturation for the major loops. For the harmonic analysis, at each field 10 phase measurements were performed and the average of the 10 measurements is represented as point on Fig. 2A and 2B. The error bars represent the standard deviation of the 10 measurements. All other data presented has been unaltered.

To demonstrate repeatability major and minor loops are presented for four different samples (Fig. S15) and for three different devices on one sample (Fig. S16).

Supporting Information

Supporting Information is available from the Wiley Online Library or from the author.

Competing Interests

The authors declare no competing interests.

Author Contributions

Experiments were developed by P.B., S.D., and R.R. STO/PTO/STO samples were grown by S.D and P.M. PTO sample was grown by P.K. PMN sample was grown by Z.T. TEM measurements were done by S.S. Devices were fabricated by E.P, L.C, and P.B. Harmonic Analysis Measurements were done by P.B., E.P, and A.F. Switching Speed Measurements were done by P.B. and E.P. PE and IV measurements were done by P.B. and S.D. Endurance Cycling was done by P.B. and P.K. *In Situ* PFM measurements were done by P.B. *Ex Situ* PFM measurements were done by V.S and P.B. Phase Field Calculations was done by Y.W. and Z.H. Second Principles Calculations were done by F.G.O and J.J. P.B., E.P., F.G.O., P.B.M, P.K., L.C., A.F., L.W.M., S.D., J.J., Z.H., and R.R. contributed to the discussion and understanding of data. Core of the manuscript was written by P.B. and R.R. All authors contributed in the preparation of the final manuscript.

Acknowledgements

P.B, S.S, and R.R acknowledge support of the U.S. Department of Energy, Office of Science, Office of Basic Energy Sciences, under contract no. DE-AC02-05CH11231. L.C. acknowledges support from the University of California Office of the President and the Ford Foundation. E.P. acknowledges support from the COFEEE and FEINMAN Programs supported by Intel Corp. P.M., L.W.M., and R.R. acknowledge support of the Army Research Office under the ETHOS MURI via cooperative agreement W911NF-21-2-0162. P.K.

acknowledges support of the Intel Corp. via the COFEEE program. Z.T. acknowledges the support of the U.S. Department of Energy, Office of Science, Office of Basic Energy Sciences, under Award Number DE-SC-0012375 for the development of superlattice materials. A.F. acknowledges the support of the Army Research Office under grant W911NF-21-1-0118. L.W.M. and R.R. acknowledge partial support of the U.S. Department of Energy, Office of Science, Office of Basic Energy Sciences, Materials Sciences and Engineering Division under Contract No. DE-AC02-05-CH11231 (Codesign of Ultra-Low-Voltage Beyond CMOS Microelectronics (MicroelecLBLRamesh)) for the development of materials for low-power microelectronics. F.G.-O., and J.J. acknowledge financial support from Grant No. PGC2018-096955-B-C41 funded by MCIN/AEI/10.13039/501100011033 and by ERDF "A way of making Europe" by the European Union. F.G.-O. acknowledges financial support from Grant No. FPU18/04661 funded by MCIN/AEI/10.13039/501100011033. Y.W and Z.H. acknowledges support by the Joint Funds of the National Natural Science Foundation of China (grant no. U21A2067, Y.W.) and the Fundamental Research Funds for the Central Universities (No. 2021FZZX003-02-03, Z.H.). Z.H. gratefully acknowledges a start-up grant from Zhejiang University.

Received: ((will be filled in by the editorial staff))

Revised: ((will be filled in by the editorial staff))

Published online: ((will be filled in by the editorial staff))

References

[1] A. K. Yadav, C. T. Nelson, S. L. Hsu, Z. Hong, J. D. Clarkson, C. M. Schlepuëtz, A. R. Damodaran, P. Shafer, E. Arenholz, L. R. Dedon, D. Chen, A. Vishwanath, A. M. Minor, L. Q. Chen, J. F. Scott, L. W. Martin, R. Ramesh, *Nature* **2016**, *530*, 198.

[2] S. Das, Y. L. Tang, Z. Hong, M. A. P. Gonçalves, M. R. McCarter, C. Klewe, K. X. Nguyen, F. Gómez-Ortiz, P. Shafer, E. Arenholz, V. A. Stoica, S. L. Hsu, B. Wang, C. Ophus, J. F. Liu, C. T. Nelson, S. Saremi, B. Prasad, A. B. Mei, D. G. Schlom, J. Íñiguez, P. García-Fernández, D. A. Muller, L. Q. Chen, J. Junquera, L. W. Martin, R. Ramesh, *Nature* **2019**, *568*, 368.

[3] Y. J. Wang, Y. P. Feng, Y. L. Zhu, Y. L. Tang, L. X. Yang, M. J. Zou, W. R. Geng, M. J. Han, X. W. Guo, B. Wu, X. L. Ma, *Nat. Mater.* **2020**, *19*, 881.

[4] Y.-T. Shao, S. Das, Z. Hong, R. Xu, S. Chandrika, F. Gómez-Ortiz, P. García-Fernández, L.-Q. Chen, H. Hwang, J. Junquera, L. Martin, R. Ramesh, D. Muller, *Microsc. Microanal.* **2021**, *27*, 348.

[5] P. Zubko, J. C. Wojdel, M. Hadjimichael, S. Fernandez-Pena, A. Sené, I. Luk'yanchuk, J. M. Triscone, J. Íñiguez, *Nature* **2016**, *534*, 524.

[6] A. K. Yadav, K. X. Nguyen, Z. Hong, P. García-Fernández, P. Aguado-Puente, C. T.

Nelson, S. Das, B. Prasad, D. Kwon, S. Cheema, A. I. Khan, C. Hu, J. Íñiguez, J. Junquera, L. Q. Chen, D. A. Muller, R. Ramesh, S. Salahuddin, *Nature* **2019**, *565*, 468.

[7] L. Louis, I. Kornev, G. Geneste, B. Dkhil, L. Bellaiche, *J. Phys. Condens. Matter* **2012**, *24*, 402201.

[8] P. Shafer, P. García-Fernández, P. Aguado-Puente, A. R. Damodaran, A. K. Yadav, C. T. Nelson, S. L. Hsu, J. C. Wojdeł, J. Iñiguez, L. W. Martin, E. Arenholz, J. Junquera, R. Ramesh, *Proc. Natl. Acad. Sci. U. S. A.* **2018**, *115*, 915.

[9] P. Behera, M. A. May, F. Gómez-Ortiz, S. Susarla, S. Das, C. T. Nelson, L. Caretta, S.-L. Hsu, M. R. McCarter, B. H. Savitzky, E. S. Barnard, A. Raja, Z. Hong, P. García-Fernandez, S. W. Lovesey, G. van der Laan, C. Ophus, L. W. Martin, J. Junquera, M. B. Raschke, R. Ramesh, *Sci. Adv.* **2022**, *8*, 8030.

[10] Q. Li, V. A. Stoica, M. Paściak, Y. Zhu, Y. Yuan, T. Yang, M. R. McCarter, S. Das, A. K. Yadav, S. Park, C. Dai, H. J. Lee, Y. Ahn, S. D. Marks, S. Yu, C. Kadlec, T. Sato, M. C. Hoffmann, M. Chollet, M. E. Kozina, S. Nelson, D. Zhu, D. A. Walko, A. M. Lindenberg, P. G. Evans, L.-Q. Chen, R. Ramesh, L. W. Martin, V. Gopalan, J. W. Freeland, J. Hlinka, H. Wen, *Nature* **2021**, *592*, 376.

[11] C. T. Nelson, Z. Hong, C. Zhang, A. K. Yadav, S. Das, S.-L. Hsu, M. Chi, P. D. Rack, L.-Q. Chen, L. W. Martin, R. Ramesh, *Microsc. Microanal.* **2019**, *25*, 1844.

[12] K. Du, M. Zhang, C. Dai, Z. N. Zhou, Y. W. Xie, Z. H. Ren, H. Tian, L. Q. Chen, G. Van Tendeloo, Z. Zhang, *Nat. Commun.* **2019**, *10*, 4864.

[13] A. R. Damodaran, J. D. Clarkson, Z. Hong, H. Liu, A. K. Yadav, C. T. Nelson, S. L. Hsu, M. R. McCarter, K. D. Park, V. Kravtsov, A. Farhan, Y. Dong, Z. Cai, H. Zhou, P. Aguado-Puente, P. Garcia-Fernandez, J. Iniguez, J. Junquera, A. Scholl, M. B. Raschke, L. Q. Chen, D. D. Fong, R. Ramesh, L. W. Martin, *Nat. Mater.* **2017**, *16*, 1003.

[14] J. F. Scott, C. A. Paz De Araujo, *Science (80-.).* **1989**, *246*, 1400.

[15] O. Auciello, J. F. Scott, R. Ramesh, *Phys. Today* **1998**, *51*, 22.

[16] T. Mikolajick, U. Schroeder, S. Slesazeck, *IEEE Trans. Electron Devices* **2020**, *67*, 1434.

[17] T. Yang, C. Dai, Q. Li, H. Wen, L. Q. Chen, *Phys. Rev. B* **2021**, *103*, 220303.

[18] D. Damjanovic, in *Sci. Hysteresis*, **2006**, pp. 337–465.

[19] B. Xu, C. Paillard, B. Dkhil, L. Bellaiche, *Phys. Rev. B* **2016**, *94*, 140101.

[20] K. Carl, K. H. Hardtl, *Ferroelectrics* **1977**, *17*, 473.

[21] M. Hoffmann, Z. Wang, N. Tasneem, A. Zubair, P. V. Ravindran, M. Tian, A. A. Gaskell, D. Triyoso, S. Consiglio, K. Tapily, R. Clark, J. Hur, S. S. K. Pentapati, S. K. Lim, M. Dopita, S. Yu, W. Chern, J. Kacher, S. E. Reyes-Lillo, D. Antoniadis, J. Ravichandran, S. Slesazeck, T. Mikolajick, A. I. Khan, *Nat. Commun.* **2022**, *13*, 1228.

[22] G. Robert, D. Damjanovic, N. Setter, *Appl. Phys. Lett.* **2000**, *77*, 4413.

[23] L. M. Riemer, L. Jin, H. Uršič, M. Otonicar, T. Rojac, D. Damjanovic, *J. Appl. Phys.* **2021**, *129*, 054101.

[24] S. Hashemizadeh, D. Damjanovic, *Appl. Phys. Lett.* **2017**, *110*, 192905.

[25] S. Trolier-McKinstry, N. B. Gharb, D. Damjanovic, *Appl. Phys. Lett.* **2006**, *88*, 202901.

[26] D. A. Hall, *Ferroelectrics* **1999**, *223*, 319.

[27] S. Shetty, J. Kim, L. W. Martin, S. Trolier-Mckinstry, *J. Appl. Phys.* **2020**, *128*, 194102.

[28] R. Pirc, R. Blinc, V. Bobnar, *Phys. Rev. B - Condens. Matter Mater. Phys.* **2001**, *63*, DOI 10.1103/PhysRevB.63.054203.

[29] A. Fernandez, J. Kim, D. Meyers, S. Saremi, L. W. Martin, *Phys. Rev. B* **2020**, *101*, 94102.

[30] H. Aramberri, N. S. Fedorova, J. Íñiguez, *Sci. Adv.* **2022**, *8*, 4880.

[31] W. J. Merz, *J. Appl. Phys.* **1956**, *27*, 938.

[32] W. J. Merz, *Phys. Rev.* **1954**, *95*, 690.

[33] P. Kavle, J. A. Zorn, A. Dasgupta, B. Wang, M. Ramesh, L. Q. Chen, L. W. Martin, *Advanced Materials* **2022**, *34*, 2203469.

[34] Parsonnet, E. ekpy (Version 0.1.11) [Computer software]. https://github.com/eparsonnet93/ekpmeasure

[35] E. N. O'Connell, K. Moore, E. McFall, M. Hennessy, E. Moynihan, U. Bangert, M. Conroy, *Microsc. Microanal.* **2022**, *28*, 1444.

[36] Y. L. Li, S. Y. Hu, Z. K. Liu, L. Q. Chen, *Acta Mater.* **2002**, *50*, 395.

[37] L. Q. Chen, *Annu. Rev. Mater. Sci.* **2002**, *32*, 113.

[38] L. Q. Chen, *J. Am. Ceram. Soc.* **2008**, *91*, 1835.

[39] Z. Hong, A. R. Damodaran, F. Xue, S. L. Hsu, J. Britson, A. K. Yadav, C. T. Nelson, J. J. Wang, J. F. Scott, L. W. Martin, R. Ramesh, L. Q. Chen, *Nano Lett.* **2017**, *17*, 2246.

[40] M. J. Haun, E. Furman, S. J. Jang, H. A. McKinstry, L. E. Cross, *J. Appl. Phys.* **1987**,

62, 3331.

[41] L. Q. Chen, J. Shen, *Comput. Phys. Commun.* **1998**, *108*, 147.

[42] J. J. Wang, X. Q. Ma, Q. Li, J. Britson, L. Q. Chen, *Acta Mater.* **2013**, *61*, 7591.

[43] J. C. Wojdeł, P. Hermet, M. P. Ljungberg, P. Ghosez, J. Íñiguez, *J. Phys. Condens. Matter* **2013**, *25*, 305401.

[44] J. C. Wojdeł, J. Íñiguez, *Phys. Rev. Lett.* **2014**, *112*, 247603.

[45] P. García-Fernández, J. C. Wojdeł, J. Íñiguez, J. Junquera, *Phys. Rev. B* **2016**, *93*, 195137.

Metastable Switching Events in Polar Vortex Arrays

Within the polar vortex lattice, low-field metastable switching events are demonstrated in coesitance with classical ferroelectric bistability. By changing the poled state of the vortex lattice one can tune the anistropy of these low-field hysteresis loops, allowing for a novel method of non-destrucive readout of the poled state with a simple in-plane capacitor.

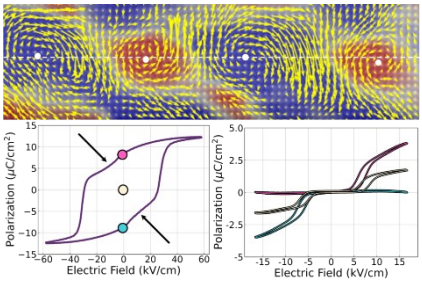

Supporting Information

Metastable Switching Events in Polar Vortex Arrays

Piush Behera[1,2], Eric Parsonnet[3], Fernando Gómez-Ortiz[4], Vishantak Srikrishna[3], Peter Meisenheimer[1], Sandhya Susarla[1,2], Pravin Kavle[1,2], Lucas Caretta[1], Yongjun Wu[5], Zishen Tian[1], Abel Fernandez[1], Lane W. Martin[1,2], Sujit Das[6], Javier Junquera[4], Zijian Hong[5], Ramamoorthy Ramesh[1,2,3*]*

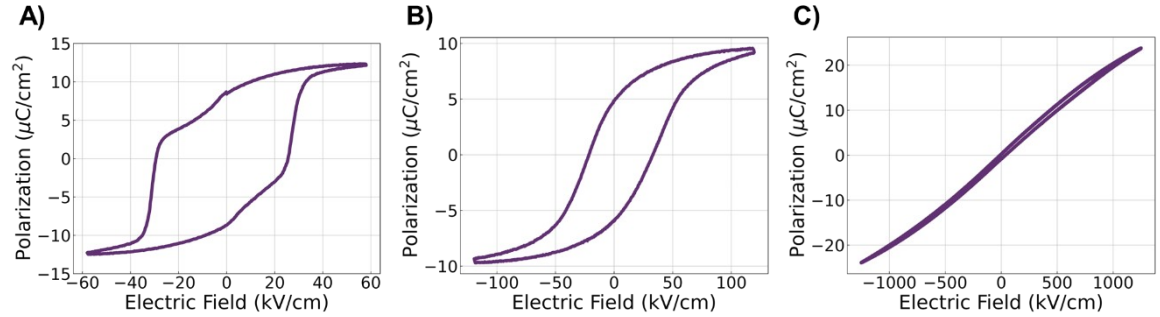

Figure S1 PE Loops along $[100]_{pc}$ (a), $[010]_{pc}$ (b), and $[001]_{pc}$ (c) direction

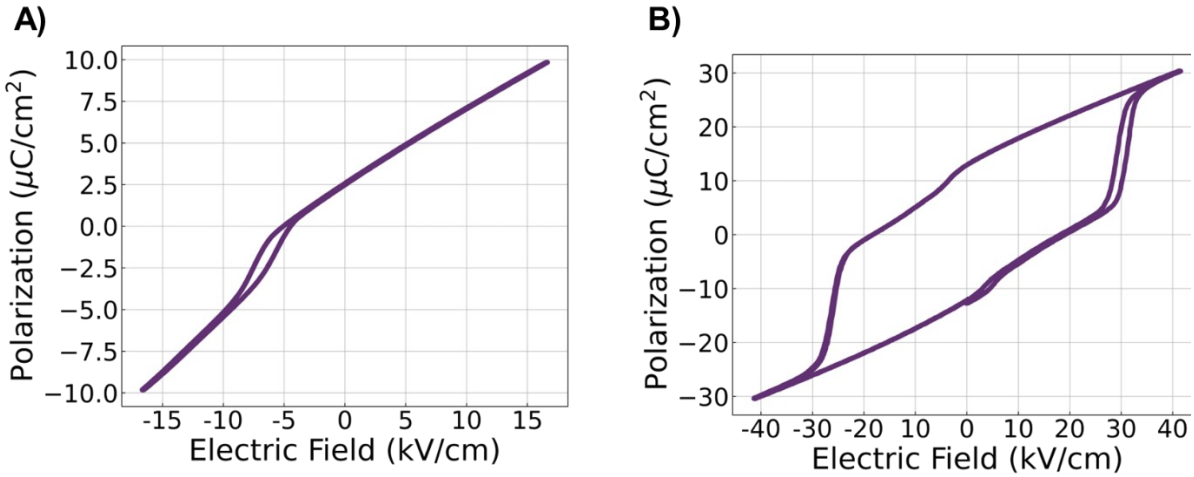

Figure S2 Raw data without subtraction of the dielectric component for the minor loop (a) and major loop (b)

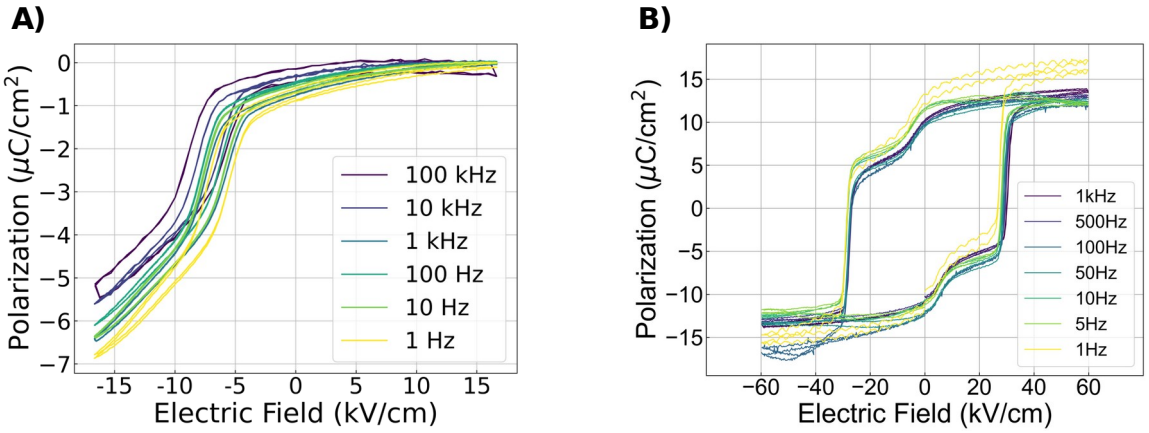

Figure S3 Frequency dependence from 1 Hz to 100 kHz for the minor loop (a) and 1 Hz to 1 kHz for the major loop (b).

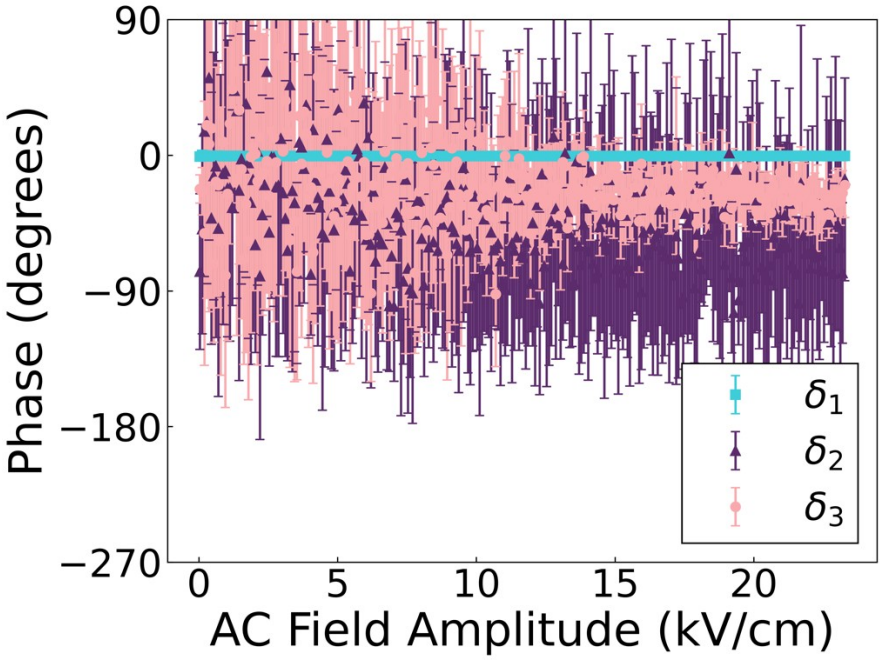

Figure S4 First three harmonics measured for a bare $DyScO_3$ substrate along the $[100]_{pc}$ direction. Data shows minimal third harmonic signal for the same fields as compared to the vortex sample.

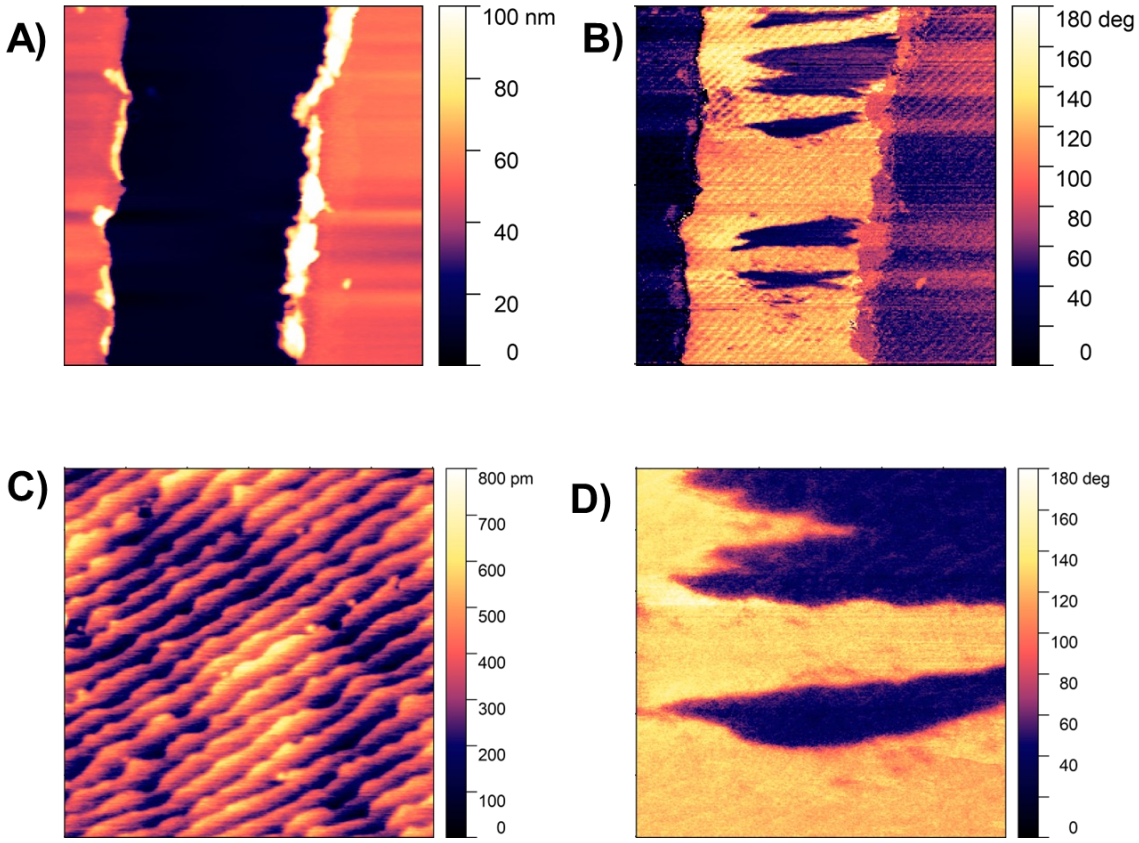

Figure S5 PFM scans of region where *in situ* PFM was performed (A) Topography of the in-plane electrodes (B) Phase channel showing domains of opposite polarization (C) Zoomed in topography showing atomic terraces (D) Corresponding PFM phase of zoomed in image.

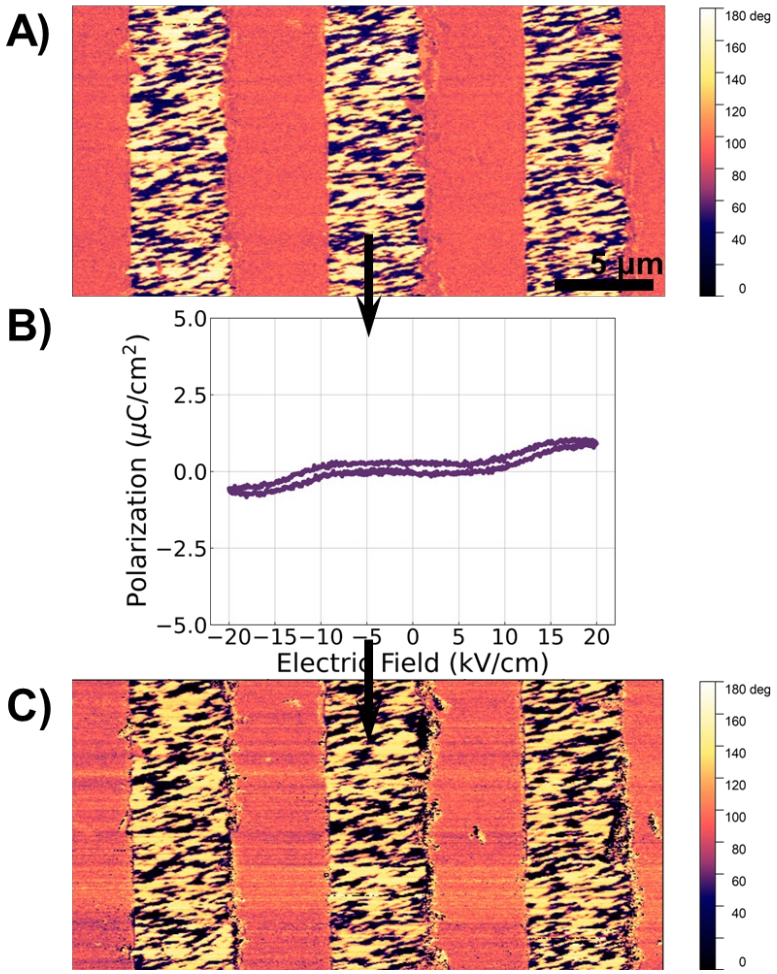

Figure S6 (A) PFM scan showing domains between in-plane electrodes (B)Minor loop taken of device after performing scan (A). (C) PFM scan taken after collection of minor loop (B). This shows no change in the overall domain structure after performing the minor loop.

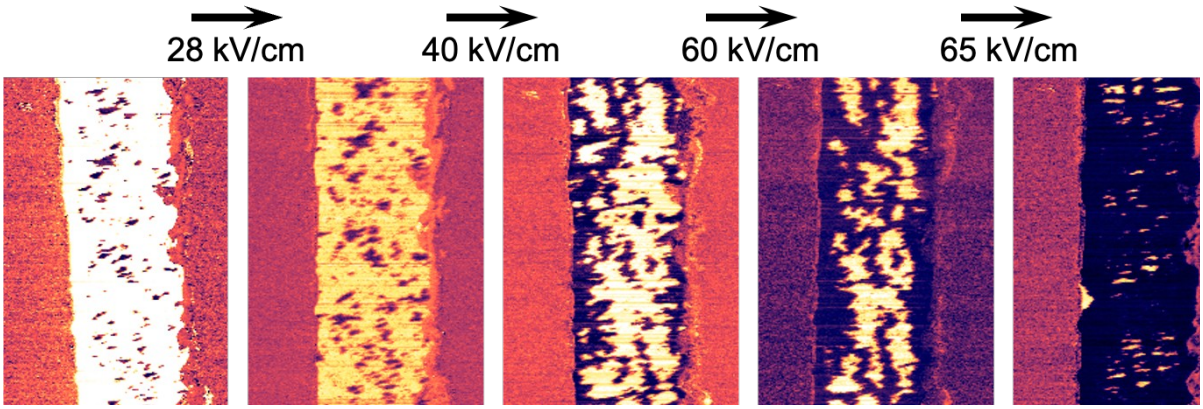

Figure S7 *Ex situ* PFM scan. Starting from a negatively poled sample images show nucleation and growth of domains upon application of large positive fields

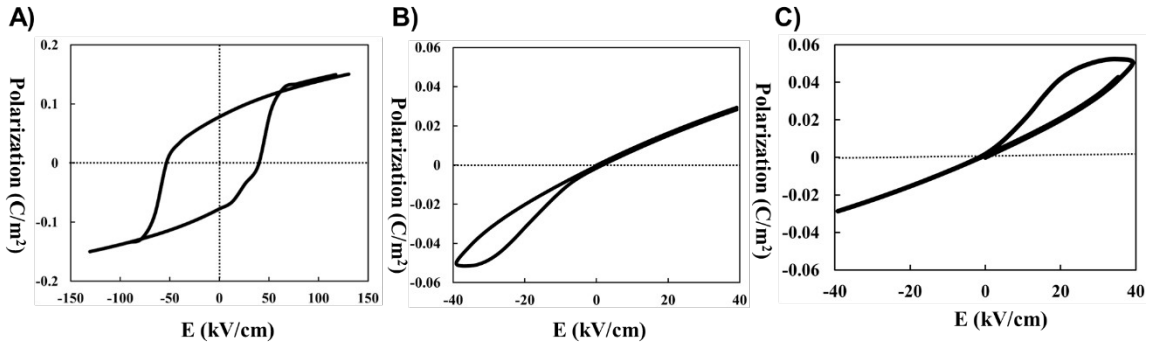

Figure S8 Phase field modelling of major loop (a), minor loop in +P state (b), and minor loop in -P state (c)

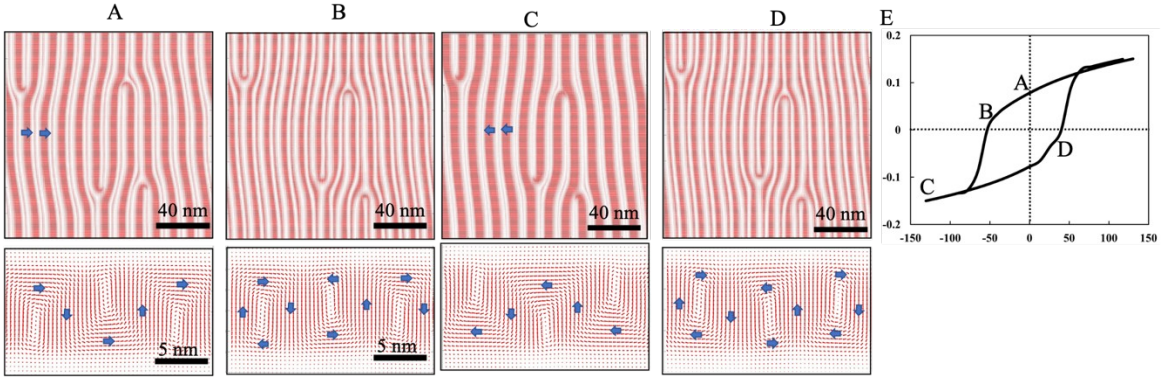

Figure S9 Phase field modelling showing plane view and cross sections at 0 kV/cm (a), -50 kV/cm (b), -125 kV/cm (c), a +50 kV/cm (D) and (E) the polarization vs. electric field hysteresis loop under high poling field (major loop).

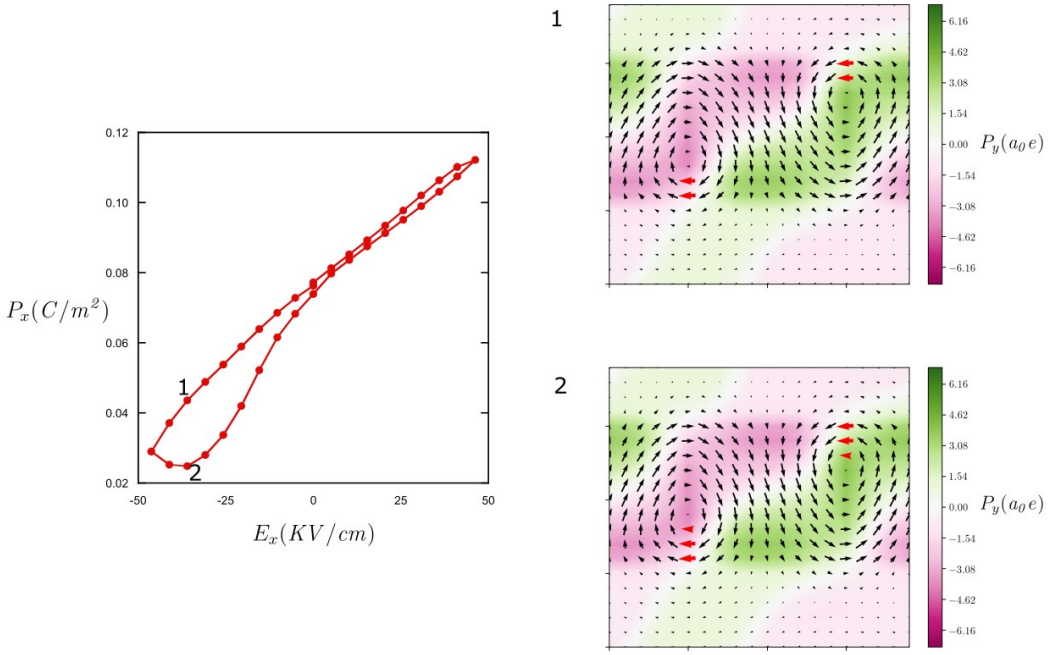

Figure S10 Second principles calculation showing (A) +*P* minor loop and corresponding cross-sectional view of vortices at loop position 1 (b) and position 2 (c). Highlighted arrows indicate how vortices are displaced slightly in the vertical direction

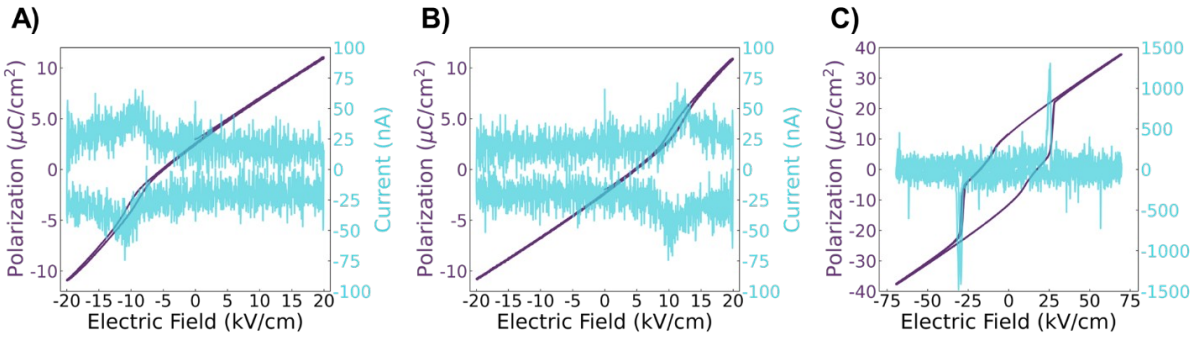

Figure S11 PE loops (purple) and current vs. electric field curves (blue) for the +*P* minor loop (A), the -*P* minor loop (B), and the major loop (C). Current vs. field curves for minor loops (A,B) were averaged over 100 loops due to minimal current.

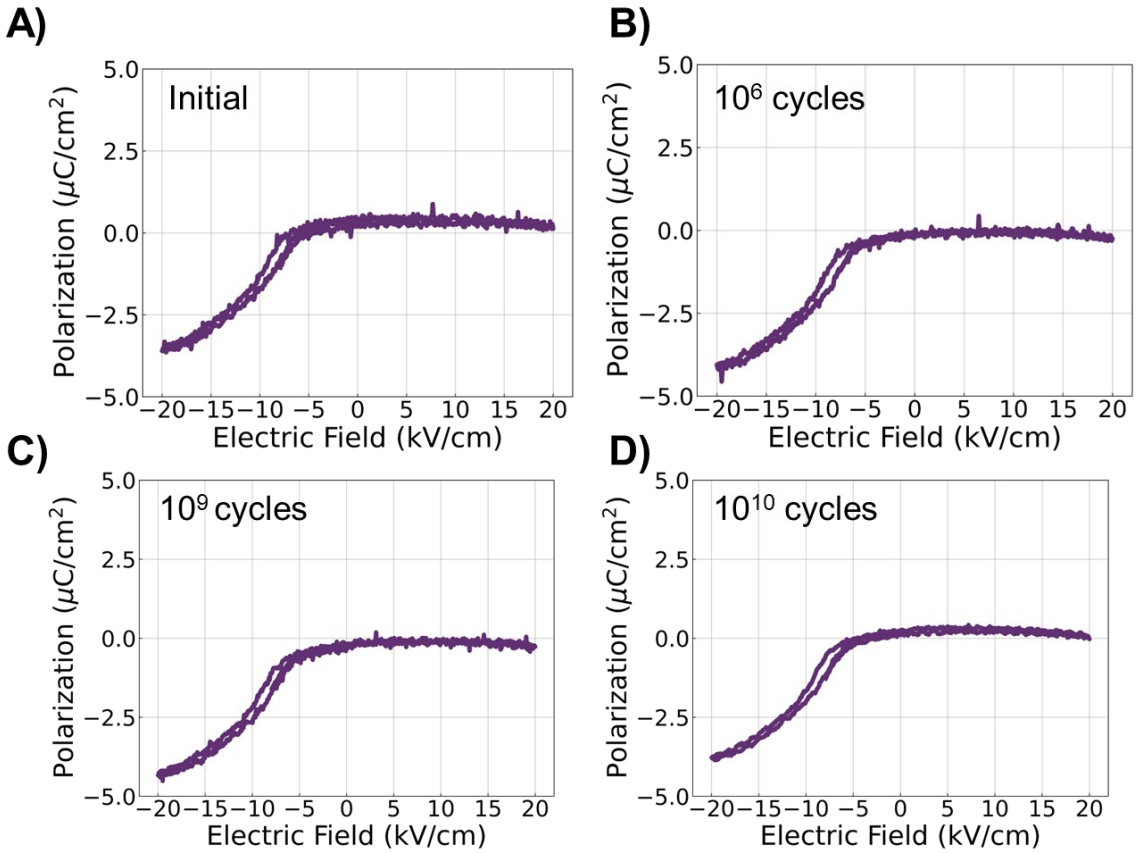

Figure S12 Endurance cycling of minor loop using a 20kV/cm, 500kHz triangular waveform. PE loops are presented for the initial state (a), after 10^6 cycles (b), after 10^9 cycles (c), and after 10^{10} cycles (d)

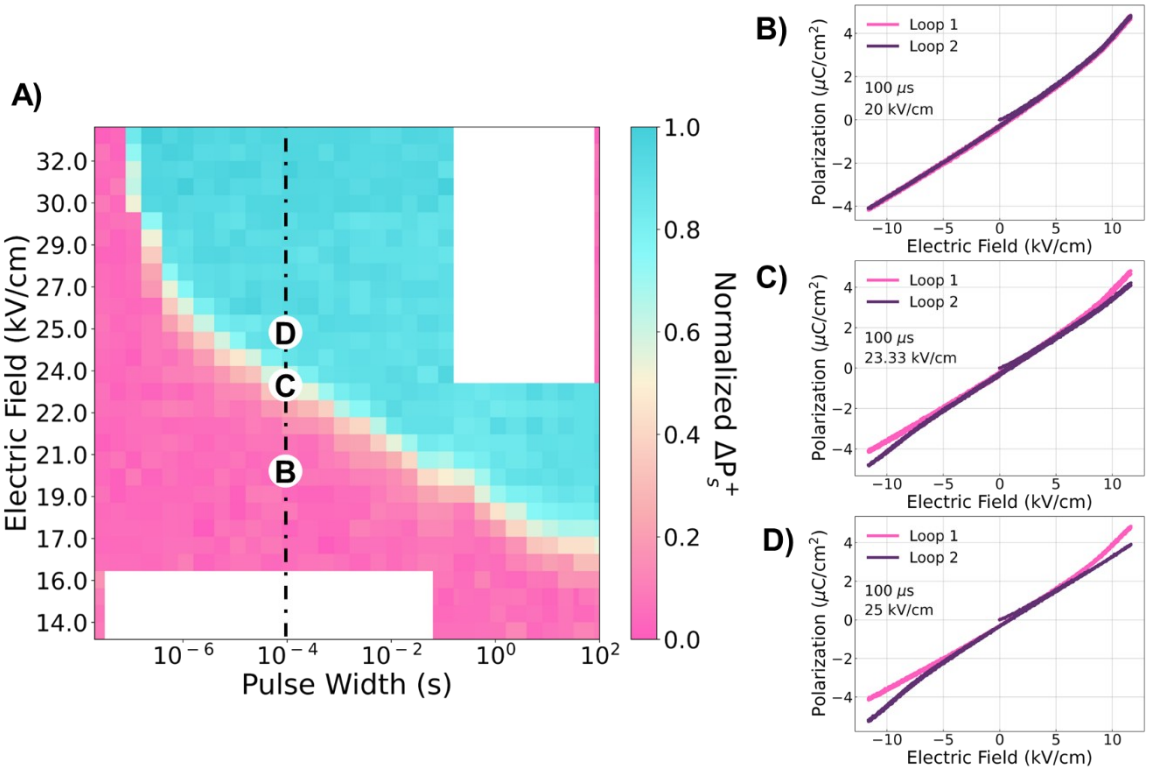

Figure S13 (a) Full switching speed study with extension to longer pulse widths of up to 100s. (b-d) Pre-switching pulse PE loop (pink/loop 1) and post-switching pulse (purple/loop 2) PE loop taken with application of a 100 μs switching pulse with amplitudes of 20 kV/cm (b), 23.33 kV/cm (c), and 25 kV/cm (d).

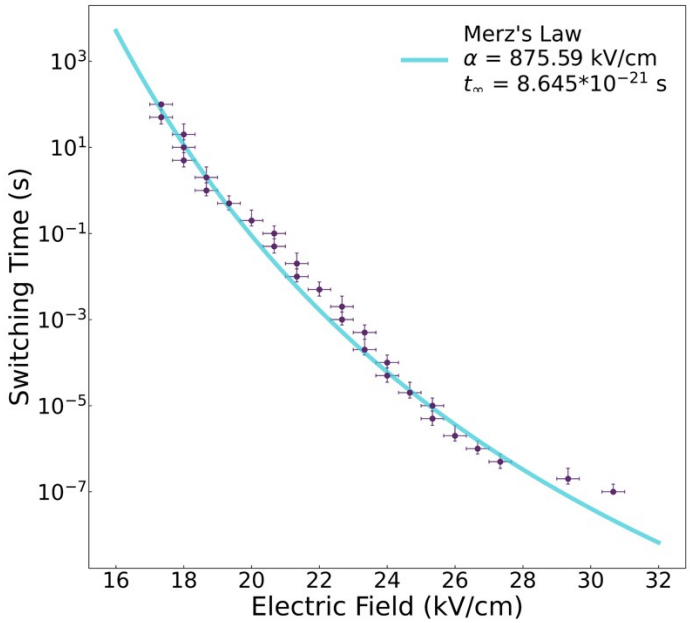

Figure S14 Switching speed versus electric field (pulse amplitude), extracted from Figure 5C as when $\Delta P_s^{+¿¿}$ is greater than or equal to 0.5. Fit is to Merz's Law

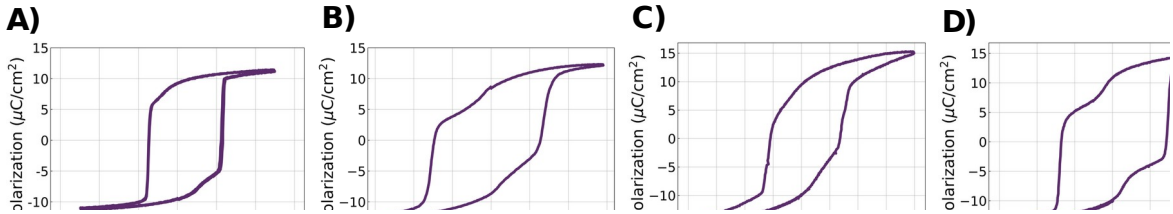

Fig. S15 (A-D) Major loops for four different $STO_{20}/PTO_{20}/STO_{20}$ samples. (E-H) Negatively poled minor loops for the same four samples.

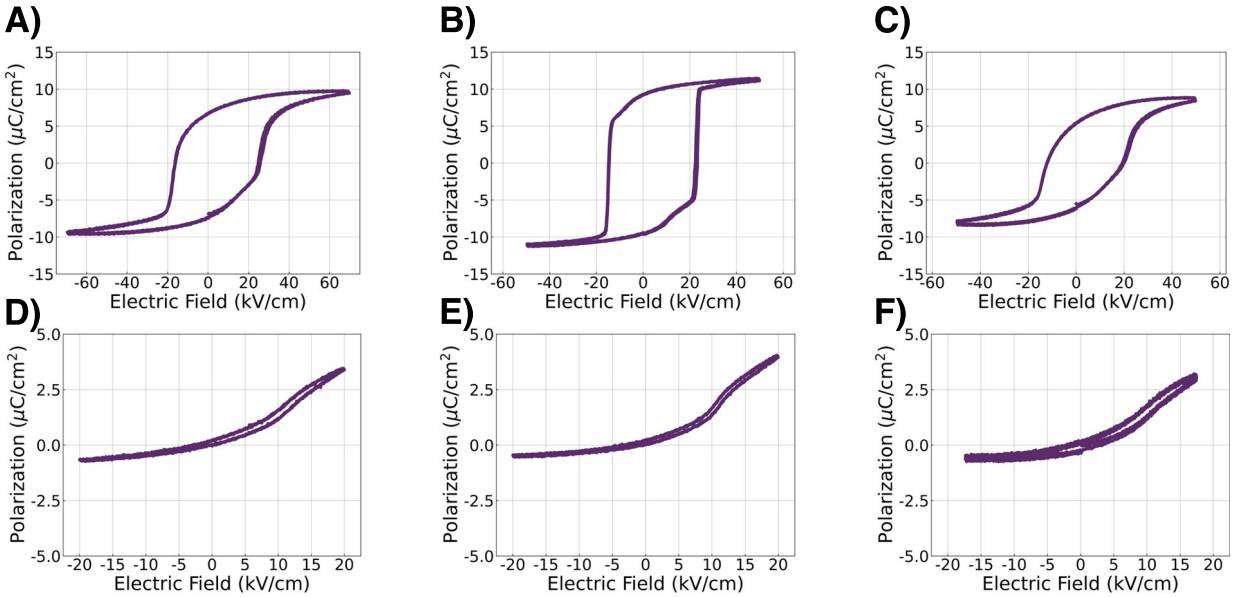

Fig. S16 Copy of Fig. S16. (A-C) Major loops for three different devices for the same vortex sample. (D-F) Negatively poled minor loops for the same three devices.

Supplementary Section A: Switching Speed vs. Electric Field

To further analyze the switching speeds, the points at which the normalized $\Delta P_s^{+¿¿}$ is greater than or equal to 0.5 are extracted, and the time versus field is plotted (Figure S14). An exponential decay is observed that is well modeled by Merz's law:

$$t_0 = t_\infty e^{\frac{a}{E}} \qquad (1)$$

where t_0 is the switching speed, t_∞ is the switching time at infinite field, α is the activation field, and E is the applied field. This is an empirically derived equation stemming from the nucleation of growth of domain walls, which describes switching behavior in classical ferroelectrics.[1,2] In this case the activation energy (α = 875.59 kV/cm) is much larger than the coercive field of the minor loop, with a ratio of ~35. Typical ratios of the activation energy to coercive field lie close to 15; however, ratios as large as 40 have been previously reported with larger ratios being indicative to larger barrier to domain-wall nucleation and growth and the presence of larger depolarization fields.[3-5]

References

1. Merz, W. J. Switching time in ferroelectric BaTiO3 and its dependence on crystal thickness. *J. Appl. Phys.* **27**, 938–943 (1956).
2. Merz, W. J. Domain formation and domain wall motions in ferroelectric BaTiO3 single crystals. *Phys. Rev.* **95**, 690–698 (1954).
3. Song, T. K. *et al.* Activation fields in ferroelectric thin film capacitors: Area dependence. *Appl. Phys. Lett.* **73**, 3366–3368 (1998).
4. Zhao, D. *et al.* Depolarization of multidomain ferroelectric materials. *Nat. Commun.* **10**, 2547 (2019).
5. Jo, J. Y. *et al.* Polarization switching dynamics governed by the thermodynamic nucleation process in ultrathin ferroelectric films. *Phys. Rev. Lett.* **97**, 247602 (2006).